applied optics

Controlling photoluminescent emission from polymer membranes through the creation of local deformation zones

PO-JUI CHEN, XUAN LONG HO, AND JONATHON DAVID WHITE*

Department of Photonics Engineering, Yuan Ze University, Zhong-Li 30203, Taiwan
*Corresponding author: whitejd@xiaotu.ca

Understanding and optimizing light propagation and extraction in light-emitting systems, such as fluorescent chemical sensors, is important for the production of more efficient sensors. We apply Monte Carlo ray tracing to model the effects of one-dimensional perturbations of film thickness on the luminescent emission (spatial, directional, spectral) of a freestanding transparent polymer film embedded with luminescent chromophores. Such modification not only enhances light extraction but also allows its location and direction to be controlled. Optimization of the deformation geometry allows for a 3.6-fold increase in intensity for a far-field detector. © 2016 Optical Society of America

OCIS codes: (120.5820) Scattering measurements; (310.6860) Thin films, optical properties; (180.2520) Fluorescence microscopy.

http://dx.doi.org/10.1364/AO.55.000576

1. INTRODUCTION

Understanding and optimizing the interaction between light propagation, extraction, scattering, and self-absorption, or in other words light management, in two-dimensional thin films is a key challenge for many applications. [1] For light-emitting diodes (LEDs), the goal is to maximize light extraction by *minimizing* light trapping. This is often accomplished by maximizing the scattering of light within the film [2,3] in order to overcome total internal reflection. For solar cells, the goal is to maximize light absorption by maximizing light trapping [4,5]. Again, this is done by maximizing the scattering of light within the film [1] to couple the light into trapped modes. For luminescent solar collectors, the goal is to maximize light propagation distances (utilizing light trapping and waveguiding) in order to maximize the number of photons reaching a high-quantum-efficiency detector [6–8]. For thin membranes acting as fluorescent chemical sensors, the goal is to maximize the change in luminescence on the detector surface in the presence of the target molecule. In all cases, the key challenge is thus to maximize the conversion of emitted light to useful outgoing energy or signal, through light management.

Within this large field, the majority of research has concentrated on light management in gallium-nitride- (GaN) based LEDs due to their commercial application. While, the internal quantum efficiency of GaN-based LEDs is already very high, its high index of refraction results in the majority of luminescence being trapped or guided within the active layer [9].

Understanding, quantifying, and enhancing the light extraction efficiency, denoted as LEE or η in the literature, through an understanding of light propagation and scattering within the active layer is thus of crucial importance [10,11]. Various methods have been employed to modify geometry in order to aid in light extraction, such as forming a nanostructured graded-index antireflection layer [12], embedding photonic crystals [13], and texturing the active layer [14]. Closely related to light extraction is the issue of light propagation within these films. As both propagation and extraction are difficult to quantify experimentally [9], recent work has focused on the use of simulation techniques such as radiative transfer analysis [15], 3D-Finite-difference time-domain [16], rigorous coupled-wave analysis (RCWA) [17,18], and Monte Carlo ray-tracing simulations [19]. The latter being used, for example, to investigate the effects of pyramidal texture [20] or implanting pyramidal lens array [9]. In work published earlier this year, Kang *et. al* investigated biomimetic structures by combining ray tracing to handle micron-sized structures with RCWA to handle 50 nm and smaller structures [21].

While light management in LEDs has been the main focus of research, the issues of light propagation and extraction are also of concern for other light-emitting systems such as membranes of luminescent polymers used as chemical sensors [22–24]. In Fig. 1(a), up to 80% of emitted light is trapped within a flat film due to total internal reflection [25]. In such systems, the presence of the target molecule quenches the

photoluminescent emission. The problem here is different from that faced in LEDs as these systems are characterized by low levels of fluorescent emission and equally low levels of self-absorption. For such sensors, the key parameter is *not* LEE but rather involves optimizing the location and/or angular direction (θ, ϕ) of emission so that it is incident on the detector. As seen in Fig. 1(a), this optimization also needs to take into account the detector geometry. For a point detector placed close to the film (i.e., the film fills the detector's field of view), it is the radiance (W/sr/m^2) that needs to be optimized. For a point detector far away from the film (as is the case in a UV–visible spectrometer), it is the radiant intensity (W/sr) or gain that one is seeking to optimize. (i.e., at large distances, the film appears as a point source). For a CCD array, one is also concerned about maximizing the radiant exitance (W/m^2) at a given location.

In this work, we apply the Monte Carlo ray-tracing technique to model the effects of a one-dimensional perturbation of film thickness on the luminescent emission (spatial and directional) of a freestanding transparent polymer film embedded with luminescent chromophores. In particular, we demonstrate, that by employing local deformation zones (LDZs), both the location and direction of emission can be controlled by making use of light trapping (and waveguiding) within the film followed by light extraction at the zone edges. LDZs can be created by stretching the film or membrane [26] or by stamping

with a one-dimensional mold [3]. In the former case, grooves in the otherwise flat film result from the application of a uni-axial strain of a few percent as minor inhomogeneities within the film result in areas of high local stress initiating the formation of LDZs. By controlling the rate of the application of strain, the separation of these LDZs can be controlled, while the amount of strain applied allows control of their width and depth. In the latter case, stamping offers even more control over the process as the groove shape can also be controlled.

2. SIMULATION DESIGN AND ANALYSIS

A. Geometry
The geometry of the modeled grooved film is illustrated in Fig. 1(b) along with the coordinate systems used in presenting the simulation results. The otherwise flat freestanding film (thickness, f) is punctuated by a periodic structure of one-dimensional grooves (LDZs) of width (w) separated by a distances. Along with width, the grooves are characterized by their thickness (g) and an edge angle (ψ). The z-axis ($\theta = 0°$) was chosen to be perpendicular to the plane of the film, and the x-axis ($\phi = 0°$) was chosen to be perpendicular to the LDZs. The values of the geometrical parameters used in this simulation are summarized in Table 1. The base geometric values are typical for spin-cast polystyrene- (PS) based films subjected to a uni-axial strain of $e = 8\%$ applied at a moderate rate. Optical parameters were for PS lightly doped with poly[2-methoxy-5-(2'-ethylhexyloxy)-pphenylene vinylene] (MEH-PPV) [27]. Excitation was modeled at $\lambda = 488$ nm (argon laser emission) and assumed to be uniform and vertical to the film (results for spot excitation have been reported elsewhere [28]). Absorption and emission dipoles were assumed to lie in the plane of the film as is typical for spin casting. [29,30] The scattering coefficient, including impurity absorption and scattering along with surface scattering, was measured using the method of Ref. [28] and set to a wavelength-independent value of 0.01 μm^{-1}. The latter parameter is highly dependent on details of film preparation.

B. Simulation Flow
Figure 2 illustrates the three-dimensional Monte-Carlo-based ray-tracing [31] algorithm used to model the emission properties of the above thin film following the absorption of an
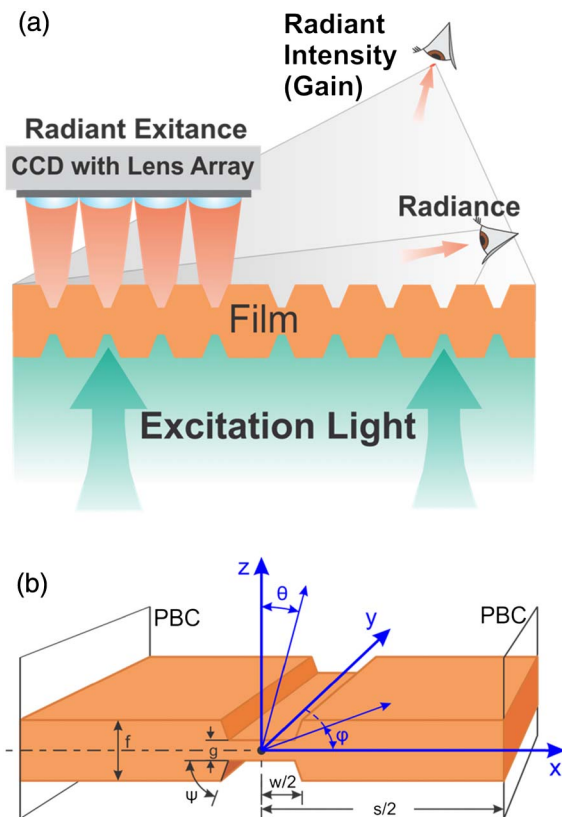
Fig. 1. Schematic of the thin film chemical sensor. (a) Location of detection optics and parameters of interest. (b) Introduction of the coordinate systems and parameters used in the simulation. *w*, width of the groove; *s*, spatial period of the structure; *f* film thickness in the bulk region; *g*, thickness in the LDZ; *ψ*, angle at the edges of the LDZ; PBC, location of the periodic boundary condition.

Table 1. Values of Geometrical and Optical Parameters Used in the Simulation

Parameter	Standard Value	Variation
Film thickness (f)	500 nm	
Groove thickness (g)	168 nm	[0500] nm
Period (s)	30 μm	[3200] μm
Groove width (w)	2.5 μm	[0.5 10] μm
Groove edge angle (ψ)	68.5°	[090]°
Index of refraction (n)	1.57	–
Absorption spectrum	dilute MEH-PPV in PS	
Photoluminescence spectrum		
Emission dipole alignment	random in the film plane (spin-cast film)	isotropic (drop-cast film)
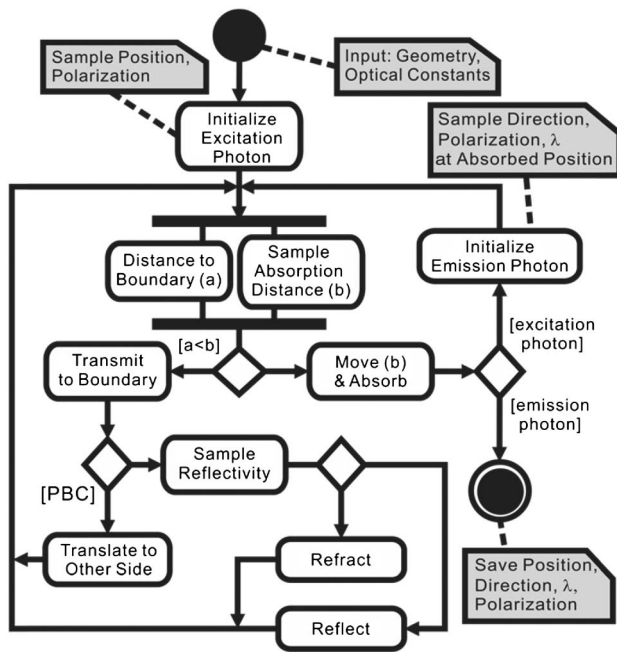
Fig. 2. Schematic illustrating the Monte-Carlo-based ray-tracing program used to follow a single-emission photon. This procedure is repeated for 10^9 excitation photons.

excitation photon. Photons (PL) were generated randomly within the membrane with wavelength, direction, and polarization properties defined by random sampling from the known photoluminescence spectra and distribution of dipole orientations. Based on the material's absorption coefficient at the generated photon's wavelength, an absorption distance (a) was assigned to the photon by sampling from an exponential decay distribution (Beer–Lambert's Law). This distance was compared to the distance to the nearest boundary (b). In the case that $a > b$, the photon was propagated a distance a, with its data stored, life ended and a new photon started. Otherwise, the photon was propagated to the boundary.

Two types of boundaries were used in the simulation: periodic (PBC) and refractive. The absorbing boundary had a reflectivity of zero, absorbing all photons that reached it. It was placed above and below the thin film to terminate the trajectory of photons that have left the film. When a photon arrived at the periodic boundary, its position was shifted to the opposite edge of the material and ray tracing continued, allowing a multiple-grooved structure to be modeled using a single groove (in the case of uniform excitation and emission). The refractive boundary was used between materials. The laws of specular reflection were considered to hold for all boundaries, i.e., there is a complete absence of scattering centers beneath the surface and within the film. The reflective angle equals the incident angle, and the refractive angle was defined by Snell's law. The probability of reflectivity (R), dependent on the relative refractive index of the materials, incident angle, and polarization, was calculated using the familiar Fresnel formulas. Whether a given photon experiences reflection or refraction was determined using a random generator to generate random value (p) uniformly distributed in the range [0 1]. For $p < R$, the

photon was reflected, while for $p > R$, transmission occurred. Each photon was followed until it was either absorbed in the film or detected by the absorbing boundary placed outside the film. In either case, the photon's polarization, position, and direction were stored for postprocessing. The simulation was implemented in C language using extensions for parallel processing and run on a standard 4-core personal computer. While the calculation of LEE requires only ten thousand rays for 1% error, one billion photons were followed to obtain the angular and spatial distribution of emission with a maximum statistical error of ∼5%. This is due to the relatively weak emission at large polar angles, i.e., parallel to the surface. We note that the results of classical ray-tracing simulations are only rigorously valid when: (1) subwavelength features do not have a major influence on the problem results, (2) the imaginary part of the refractive index is not significant, and (3) coherence effects are not significant. As photoluminescence is incoherent, the third criteria is satisfied. Considering the second, Chang *et al.* [32] have shown that the validity of this methodology depends on the ratio $x = \kappa/n$, where κ is the extinction coefficient and n is the index of refraction. When polarization information is required, the simulation is valid for $x < 0.01$. If polarization is not required, $x < 0.07$ is sufficient. For the films investigated here with a few percent weight doping of MEH-PPV, $n = 1.5$ and $\alpha < 0.16$ µm^{-1} corresponding to $x = \alpha\lambda/4\pi n$ <0.003, which is clearly within the range of the ray-tracing model's validity. Considering the first criteria, we checked the base case (depth = 167 nm) simulation results experimentally and found the simulation and experimental results were in good agreement as will be discussed in the results section.

C. Analysis Methodology

In analyzing the emission from the thin film, we are primarily interested in the overall light extraction efficiency, emission spectrum, directivity of the radiation, and physical location of emission. In antenna theory, if the radiation pattern is denoted as $p(\theta, \phi)$, then we can introduce directivity [33] as

$$D(\theta, \phi) \equiv \frac{P(\theta, \phi)}{P_r/4\pi}. \tag{1}$$

which is defined as the ratio of the radiant or radiation intensity $p(\theta, \phi)$ to the total radiated power, that is,

$$P_r \equiv \iint p(\theta, \phi) \sin \theta \mathrm{d}\theta \mathrm{d}\phi. \tag{2}$$

per unit solid angle. Again, in analogy to antenna theory, we define the gain (G) of our film as the ratio of the output power to the total input power that is to be radiated per unit solid angle. G and D are thus related by the LEE (η) of the thin film as follows:

$$G(\theta, \phi) = \frac{p(\theta, \phi)}{(p_r + P_{nr})/4\pi} = \eta D(\theta, \phi). \tag{3}$$

where P_{nr} is the fraction of the power that does not escape the membrane. In our case, we are primarily interested in the enhancement in radiation relative to the flat film and thus we define an addition parameter, enhancement,

$$\zeta(\theta, \phi) = \frac{G_{\text{LDZ}}(\theta, \phi)}{G_{\text{flat}}(\theta, \phi)}. \qquad (4)$$

as the ratio between the film with local deformation zones and the unperturbed films. We note that the plot of directional dependence of enhancement is qualitatively the same (except for units) as that of radiance due to the fact that the emission from the flat film is nearly Lambertian (uniform radiance).

While not stated explicitly, the above parameters, as in antennas, have frequency (wavelength) dependence, which results in an angle-dependent shift in the emission spectra. In order to analyze the angular-dependent changes introduced by surface geometry on the emission spectra, we make use of the spectral coefficient S_o defined in Ref. [34] as

$$S_o(\theta, \phi) = \frac{\int_{\lambda_o}^{\infty} I_e(\theta, \phi, \lambda) \mathrm{d}\lambda - \int_0^{\lambda_o} I_e(\theta, \phi, \lambda) \mathrm{d}\lambda}{\int_{\lambda_o}^{\infty} I_e(\theta, \phi, \lambda) \mathrm{d}\lambda + \int_0^{\lambda_o} I_e(\theta, \phi, \lambda) \mathrm{d}\lambda}. \qquad (5)$$

where I_e is the radiant intensity and $\lambda_o = 560$ nm (near the midpoint of the emission spectrum of MEH-PPV). Spectra that are blueshifted (redshifted) relative to the flat film will have values of S_o less (greater) than that for the flat film. (Experimentally, this corresponds to the common single molecule technique of splitting the emission spectra between two APDs by a dichroic filter [34].) In our simulation, the photons emitted within each steradian (sr) are divided into two bins, based on whether their wavelength is greater or less than 560 nm. The spectral coefficient is then calculated using Eq. (5).

3. RESULTS

A. Standard Case

In this section, we will first introduce the results for the parameters indicated in Table 1 listed under the column "Standard Value." In subsequent sections, we will investigate the effects of varying these parameters on emission. These parameters were chosen to match necking parameters obtained when stretching thin PS films. As this geometry is easily reproducible experimentally, simulation results could be verified. Two types of experiments were performed to verify simulation: uniform and spot excitation. Emission intensity (as measured using an Andor EM-CCD) closely fit predictions from simulation. The spectral coefficients (S) of the two films (measured at two different angles using a Perkin–Elmer VIS Spectrometer) were found to $S_{\text{flat}}(60°, 0°) = 0.3$, $S_{\text{flat}}(60°, 90°) = 0.3$, $S_{\text{LDZ}}(60°, 90°) = 0.36$, and $S_{\text{LDZ}}(60°, 0°) = 0.42$, which is in agreement with simulation and indicating the directional independence of spectra for the flat film and the directional dependence for the film with LDZs. Similarly, the localized intensity and spectral coefficient of emission at an LDZ was monitored as a laser spot was moved from 1 to 55 μm away from the LDZ. Both the drop of intensity and change in spectral coefficient were in accord with the predictions of the ray-tracing simulation—including the transition from increasing to decreasing in S at large distances. These results lead us to conclude that, overall, the results of the ray-tracing simulation are reliable.

Table 2 compares the LEE for a drop-cast, spin-cast, and spin-cast film with LDZs along with the enhancement effect contributed by the LDZ. The spin-cast film has a slightly

Table 2. Light Extraction Efficiency and Peak Gain for Weakly Fluorescent Films

Film	LEE(η)	η/η_{spin}	G_{peak}	$G_{\text{peak}}(\theta, \varphi)$
Drop-cast	0.23	0.85	0.40	(0°,–)
Spin-cast	0.27	1.0	0.51	(0°,–)
Spin-cast with LDZ	0.44	1.6	0.68	($30 \pm 6°$, $15 \pm 15°$)

higher LEE than the drop-cast film due to the horizontal alignment of emission dipoles induced by the spin-casting process. Comparing the LEE for the flat spin-cast film with that for the film containing LDZs spaced 30 μm apart, one can see that the incorporation of LDZs into the film has led to a ∼60% increase in the LEE from 27% to 44% of the generated irradiance. It should be noted that the absolute values of these numbers will vary with individual films due to variations in surface roughness and scattering within the films.

Figure 3 presents the PL intensity as a function of position for the grooved film plotted relative to the flat film under the case of uniform excitation. Far away from the LDZ, emission intensity is similar to that of the flat film. However, as one approaches to within 750 nm of an LDZ, radiant emittance starts to increase dramatically, reaching a factor of 9.5 times that of the unperturbed film at the edges of the LDZ. Within the LDZ, emission intensity drops but remains higher than that of the thicker film. This indicates that the increase in LEE is due primarily to light escaping from the edges of the LDZs. This localized extraction of light suggests that by focusing a detector array on the LDZs, the signal-to-noise ratio can be increased dramatically from the flat film case.

For a point detector collecting light placed far from the film, one is more interested in the changes to the radiation pattern than one is in the microscopic location of the emission. Figure 4 compares the angular distribution of the gain (qualitatively equivalent to the radiant intensity (I_e) [W/Sr] emitted from the film and enhancement (ζ) relative to a Lambertian
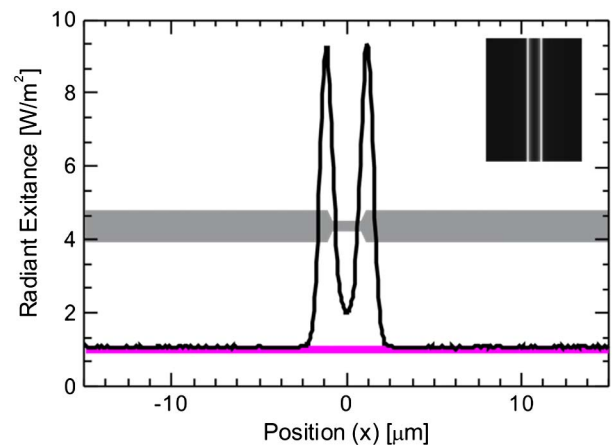
Fig. 3. Dependence of radiant exitance (W/m²) on location for the film with LDZ. Emission intensity of the grooved film (black line) is relative to that of the flat film (magenta line) which is set equal to 1 (W/m²). The cross section of the grooved film is superimposed on the graph in gray. (Inset) Simulation output (grayscale).

(a) Gain

(b) Radiance (W/sr/m²)

(c) Spectral Coefficient
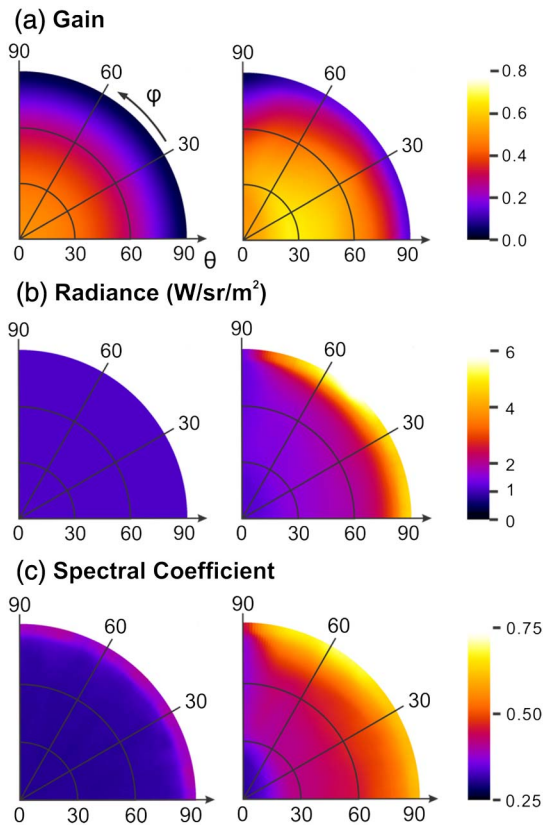
Fig. 4. Comparison of the angular dependence of photoluminescence and spectral coefficient for light emitted from flat films (left) and grooved (right). Left images illustrate the near-Lambertian emission from the flat film, while right images illustrate emission from the grooved film. (a) Gain [$G(\theta,\phi)$] of the two films, (b) radiance (W/sr/m²) (or enhancement ζ relative to a Lambertian emitter), and (c) spectral coefficient (S_o). Scale bars are on the right side of the figure.

emitter (qualitatively equivalent to radiance (L_e)[W/Sr/m²]) before and after the creation of LDZs. We first consider the flat film. The flat film gain [Fig. 4(a), left] has no ϕ dependence and is highest vertical to the film ($\theta = 0°$–$15°$, $G = 0.51$), drops slightly from $\theta = 15°$–$30°$, and then drops more rapidly to $G = 0.08$ in the range $\theta = 75°$–$90°$. In contrast, for the film with LDZs, gain [Fig. 4(a), right] is dependent on ϕ and is increased, relative to the flat film, for all angles. In addition, the gain profile is considerably flattened in the θ direction with a similar level of gain seen out to $\theta = 70°$ due to a larger increase of gain at higher emission angles. The gain maximum is no longer perpendicular to the film but slightly offset from the vertical occurring over a broad range ($\pm 1\%$) at $G(24°$–$36°, 0$–$30°) = 0.68$. This represents an increase in signal for a detector placed at this position of $\sim 40\%$ relative to the maximum signal of the flat film (detector located vertical to the film). This value is considerably less than what one would predict if one only considered LEE as a whole. The azimuthal angle dependence is due to the fact that the LDZs have little efficacy in extracting light emitted in directions of large ϕ. The shift in polar angle is due to a trade-off between the higher innate emission (flat film) in the vertical direction combined with

the greater change in emission at large polar angles (LDZ), as will be discussed in terms of radiance in the following paragraph.

This θ-dependent increase in emission is seen clearly, when one looks at the enhancement of gain (ζ) and radiance. For a detector placed close to the film, radiance is the relevant parameter. In Fig. 4(b), the change in radiance between the two films is presented. Since for a perfectly.

Lambertian emitter radiance is independent of angle, for comparison purposes, we have set the radiance of a Lambertian film to 1.0. For the flat film, emission deviates by less than $\pm 10\%$ from that expected for a Lambertian emitter (slightly higher emission is perpendicular to the film). This slight deviation is due to the horizontal rather than isotropic distribution of dipole moments induced by spin casting [29,30]. In contrast, while emission from the perturbed film is enhanced at all angles, the degree of enhancement is dependent on both polar and azimuthal angles [Fig. 4(b), right]. At large values of ϕ, parallel to the grooves, the dependence of gain on θ, while higher, is similar to that of the flat film (within $\sim 30\%$ higher). However, perpendicular to the grooves (low ϕ), the enhancement of gain is more pronounced and ranges from 1.1 vertical to the film to ~ 5 parallel to the film surface. Interestingly, maximum enhancement ($\pm 1\%$) is more narrowly focused than the gain maximum occurring at $\zeta_{max}(88°$–$90°, 46°$–$52°) \sim 6$. Not unexpectedly, the LDZs have the most influence on extraction at large polar angles (a region in which very few photons are emitted in a flat film). Considering the (θ, ϕ) dependence of radiance, and assuming a detector with NA = 0.17, the ideal angle to place it would be at ($\theta \sim 85°$, $\phi \sim 50°$). This is somewhat surprising, as a first guess would suggest that the greatest enhancement of light would be near the film surface and *perpendicular* ($\phi \sim 0°$) to the LDZs.

Accompanied with the change in gain, there are also changes in the observed spectrum. Figure 4(c) presents the spectral coefficients as a function of angle for the two films. For the flat film, the spectra is independent of angle with the exception of a slight redshift at very high values of the polar angle. The spectral coefficient S has a value of 0.3 over much of the angular range. In contrast, the spectra for the film with LDZs are slightly redshifted relative to the flat films with S ranging from $S = 0.3$ to $S = 0.7$ and is a relatively complicated function of both angles. The maximum spectral shift ($S_{max} = 0.7$) occurs at large polar angles ($> 85°$) and is similar over a large range azimuthal angles ($21°$–$80°$) overlapping with the direction of maximum radiance. The spectral shift coefficient corresponds to a shift in the spectral peak of ~ 3 nm for light emitted parallel to the grooves to ~ 6 nm for light emitted perpendicular at a polar angle of $60°$. This overall redshift is a direct result of lower absorption at longer wavelengths allowing proportionately more long wavelength light to travel within the film to reach an LDZ and have the opportunity to escape the film.

B. Effect of Varying LDZ Parameters on Emission from the Thin Film

We will now investigate the effects on gain, radiance, and light extraction of varying the key parameters defining the LDZs. In particular, the effects of depth (d), width (w), separation (s), and edge angle (ψ) of the LDZs on the thin film's emission.
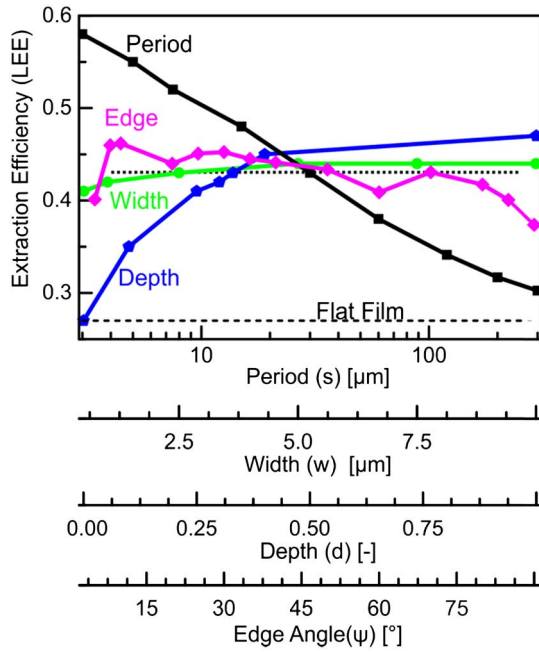
Fig. 5. Effects of varying the period, width, edge angle, and depth of the LDZ on the overall LEE (η). The lower dashed line represents the extraction efficiency of the flat film, while the upper short dashed line indicates the parameters used in the base case simulation.

Fig. 6. Effects of varying the period on the spectral coefficient. The dashed line represents the extraction efficiency of the flat film. The spectral coefficient has been integrated over all angles.

Figure 5 illustrates the effects of varying each of the above parameters individually on the overall LEE (η). Varying the width (green line) of the LDZs has little effect on extraction efficiency. The choice of edge angle (fuchsia) has some effect. LEE is a maximum for a gradual perturbation ($\psi \sim 10°$), dropping gradually by about 10% as the angle increases to $\psi \sim 80°$ and then falling rapidly as the angle approaches 90°. We note that a similar lack of enhancement has been reported by Sun's group for well structures in GaN-based light-emitting diodes [35]. Of these four parameters, only two affect LEE: the depth and the period of the LDZs. On one hand, LEE initially increases rapidly with groove depth, starts to level off at ~25% of film thickness, and saturates for depths greater than 40% of the film thickness, suggesting that this depth is sufficient to extract the majority of the light reaching an LDZ. On the other hand, LEE decreases logarithmically as the period (s) increases, reflecting Beer–Lambert's law. For this simulation, using the absorption properties of dilute MEH-PPV in PS, LDZs placed more than $s > 200$ μm apart are unable to significantly enhance light extraction, while closely spaced ($s \sim 3$ μm) can more than double the light extraction efficiency of the flat film reaching a maximum of almost 60%. This logarithmic dependence on extraction efficiency suggests that we can model the effect of a change in concentration of the chemically reactive, fluorescent molecules by a similar change periodic structure, i.e., a doubling of the doping from 1% to 2% should have the same effect on extraction efficiency as halving the period. In contrast to the other parameters, the periodicity of the LDZs also affects the emission spectrum (Fig. 6), which is increasingly redshifted as the period increases. For $s > 30$ μm, the process is reversed and the peak position gradually shifts back to its normal position as
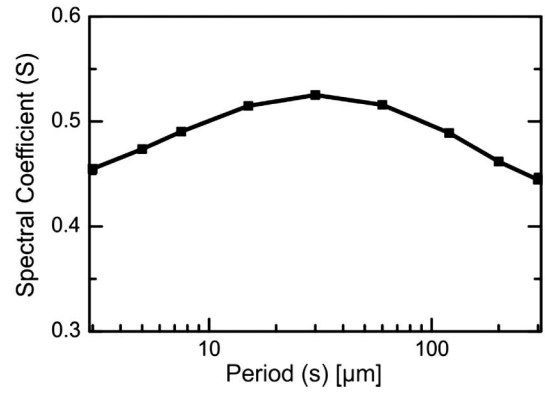
the LDZs fail to extract a significant amount of radiation. There is little connection between these two parameters.

Groove width (w) has a major qualitative affect on the positional dependence of PL emission. Figure 7 presents the radiant emittance as a function of position for LDZs of various widths. As the groove width decreases, the emission from the two edges merge into one spot giving a peak radiant emittance of close to twenty times that of the flat film for groove widths of ~0.5 μm. This represents over an order of magnitude enhancement of signal for applications in which the optics are designed to collect light from a localized area of the film. In addition, periods of the LDZs (s) will have a major effect on peak emittance with higher values of peak emittance seen for longer periods.

Finally, we consider the optimization of the directionality of the radiation. While the edge angle of the LDZs has only a moderate effect on LEE, by tuning the edge angle (ψ) of the grooves, the directionality of the emission can be modified as can the value of the peak gain. While the complete directional dependence of the gain and radiance on edge angle (ψ) is presented in Supplementary Visualization 1 and Visualization 2, Fig. 8 summarizes the effect of edge angle on the direction and magnitude of maximum gain and peak radiance. Considering first Fig. 8(a), peak gain is consistently
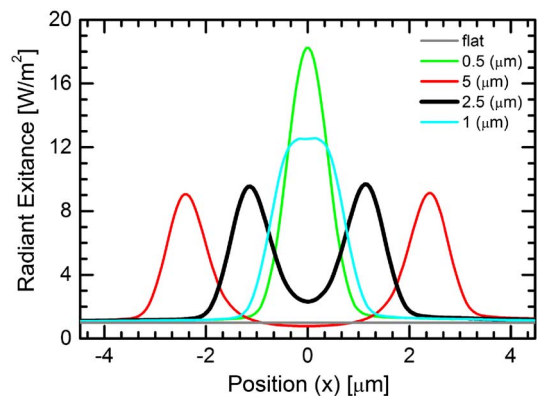
Fig. 7. Dependence of radiant exitance on location and width of the LDZs is plotted relative to that of the flat film.
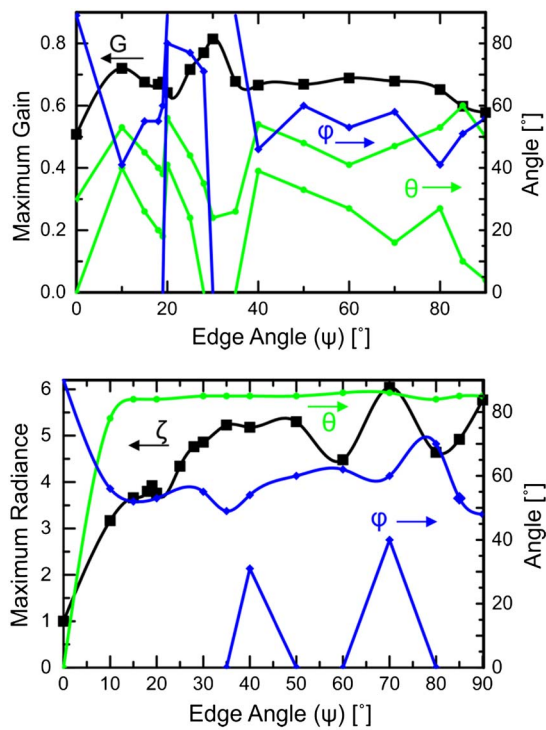
Fig. 8. Effect of the angle of the groove on the angular dependence of the emitted PL. The solid black line with squares gives (a) the maximum gain and (b) radiance. Blue diamonds and lines (green circles and lines) are the polar (azimuthal) angles for which the gain has dropped 10% from its peak. (Visualization 1 and Visualization 2.)

fluctuates between 0° and 45°, while the azimuthal angle alternates between 0° and 90°. This directional dependence allows considerable flexibility in the placement of a far-field detector.

Moving on to radiance [Fig. 8(b)], it is seen to generally increase with increasing edge angle reaching ~6.1 times that of the flat film at large edge angles. Not unexpectedly, the increase is strongest at high polar angles over a large range of azimuthal angles being maximum perpendicular to the direction of the LDZ except at edge angles of $\psi = 40°$ and $\psi = 70°$ where the maximum shifts to $\phi = 45°$ relative to the LDZs. The latter represents a maximum for the radiance. Thus, in order to maximize radiance in a given direction, it is necessary to use a relatively sharp edge angle, which is in contrast to the relatively gentle edge angles necessary to optimize gain.

C. Optimization

The above work allows us to localize our search for the parameters to maximize the gain that can be achieved for detection set up far from the film with NA = 0.13 collection optics. From Fig. 5, we expect that the maximum extraction efficiency should lie with closely spaced LDZs having a groove depth greater than 50% of the film thickness. Figure 5 indicates that the maximum light extraction efficiency occurs at $\psi = 10°$ or below. Clearly, there is a trade-off between the depth and ψ because a gentle slope of the edge will result in shallower grooves when the period is short. From Fig. 8, the maximum gain occurs with an edge angle of $\psi = 30°$ and a detector placed perpendicular to the film. (The peak at $\psi = 10°$ with a detector placed $\theta = 45°$ to the film surface represents a local maximum that needs also be considered.) Taking these as guidelines, a number of simulations were carried out. Figure 9 illustrates the angular distribution of the gain under simulations designed to optimize gain and LEE along with schematics of the film structure. Detailed geometrical parameters for these simulations are presented in Table 3 along with resulting LEE and peak gains.

For the film with $\psi = 10°$ (film a), the best LEE was a respectable 2.3-fold greater than the flat film. The high-gain region occurs over a large range of polar ($\theta = 35°$–80°) and azimuthal angles, appearing like a belt on the image [Fig. 9(a)], and the peak gain is $G_{max}(\theta, \varphi) = (54°, 51°) = 1.12$, corresponding to a factor of 2.2 improvement over the flat film. Although $\psi = 10°$ is able to achieve high LEE, farther improvement in LEE is limited by the gentle slop which restricts the depth and/or period of the LDZs. Maximum gain is limited

>25% higher than for the flat film and is largely independent of edge angle for $\psi > 40°$, while at low angles one can see that there are two peaks in the gain, one local maximum for an edge angle of $\psi = 10°$, and an overall maximum for an edge angle of $\psi = 30°$. For the flat film $G_{max,flat}(0°, –) = 0.50$, the grooved films have maximum gains of $G_{max}(45°, 20°) = 0.72$ and $G_{max}(0°, –) = 0.82$ for edge angles of $\psi = 10°$ and $\psi = 30°$, respectively. The latter peak represents a 75% increase in gain relative to the flat film. Considering the direction of peak gain, it is seen to be related to angle in a nontrivial way for both the polar and azimuthal angles. In Fig. 8(a), the direction of peak gain is delineated by lines indicating the angles at which gain has dropped by 10% from the peak. For edge angles $\psi > 40°$, the peak gain is found at $\theta \sim 35° + / – 10°$, with $\phi < 50°$. For gentler slopes, the polar angle at which the peak gain occurs

Table 3.   Selected One-Dimensional LDZs Designed to Optimize Maximum Gain and Overall Extraction Efficiency along with the Resulting Enhancement in LEE and the Maximum Gain

Film	Ψ [°]	s [μm]	w [μm]	g [nm]	LEE	LEE/LEE$_{flat}$	G_{max}	$G_{max}/G_{max,flat}$
Flat	0	∞	0.00	0	0.27	1.00	0.51	1.0
Base	68.5	30	2.50	168	0.44	1.63	0.68	1.3
a	10	2.50	2.50	22	0.62	2.30	1.12	2.2
b	30	2.50	2.50	168	0.58	2.16	1.48	2.9
c	30	2.50	2.50	100	0.59	2.20	1.69	3.3
d	30	1.00	1.00	100	0.63	2.35	1.82	3.6
e	30	0.85	0.85	0	0.66	2.44	1.33	2.6
f	30	0.29	0.29	168	0.58	2.16	1.55	3.0
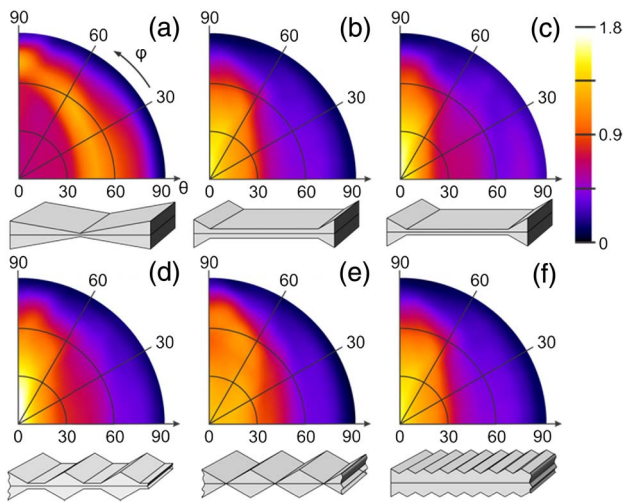
Fig. 9. Selected one-dimensional LDZs designed to optimize gain and overall extraction efficiency. The polar angle (θ) is plotted as the radial ordinate, while the azimuthal angle (ϕ) is plotted as the polar ordinate on the polar graph. (Insets) Key geometrical parameters. (Further details of the simulation conditions are in Table 3.)

by the inability of the gentle slope to focus emission in a specific direction.

The peak gain of for the film with LDZs having an edge angle $\psi = 30°$ is directed vertical to the film [Figs. 9(b)–9(f)]. For the same 2.5 mm period and 2.5 mm width of LDZs, the $\psi = 30°$ edge-angled LDZs (film *b*), although having a lower LEE (0.58 versus 0.62) than the $\psi = 10°$ LDZs, provide more focused emission allowing peak gain to be increased a factor of 2.9 times with respect to the flat film. In addition, sharpening the edge angle allows the period to be further reduced while maintaining the depth of the LDZs. The latter films, (c)–(f) in Fig. 9 and Table 3, investigate the effect of varying groove depth, period, and width of the grooved regions while maintaining the edge angle on gain distribution and LEE. The maximum peak gain was found for film *d* and corresponded to a 3.6-fold improvement on the flat film. This was found by reducing the period of the LDZs while maintaining the depth of the LDZ. As seen for film (*e*), where the period is further reduced and the film made discontinuous, any attempt to eliminate the flat structure at the bottom of the LDZ resulted in a defocusing of the gain and hence lower peak gain. Finally, as the period is further shrunk (film *f*) resulting in shallower LDZs, LEE also starts to fall off rapidly.

4. CONCLUSIONS

In conclusion, the introduction of one-dimensional LDZs in weakly fluorescent membrane's allow for a significant increase in the quantity of light extracted (up to 240% relative to a flat film), control of the location of light emission, as well as its directionality at the same time introducing a periodicity-dependent and directionally dependent redshift in the emitted photoluminescence. Tuning of the periodicity, depth, and shape of the LDZs allow one to increase the intensity on a far-field detector a factor of 3.6-fold over that obtained from a flat film. Such a perturbation to the membranes used for fluorescent chemical detection should increase sensitivity at little additional cost.

REFERENCES

1. M. L. Brongersma, Y. Cui, and S. Fan, "Light management for photovoltaics using high-index nanostructures," Nat. Mater. **13**, 451–460 (2014).
2. C.-H. Chang, K.-Y. Chang, Y.-J. Lo, S.-J. Chang, and H.-H. Chang, "Fourfold power efficiency improvement in organic light-emitting devices using an embedded nanocomposite scattering layer," Org. Electron. **13**, 1073–1080 (2012).
3. H. Hlaing, X. Lu, T. Hofmann, K. G. Yager, C. T. Black, and B. M. Ocko, "Nanoimprint-induced molecular orientation in semiconducting polymer nanostructures," ACS Nano **5**, 7532–7538 (2011).
4. S. Eyderman, S. John, M. Hafez, S. S. Al-Ameer, T. S. Al-Harby, Y. Al-Hadeethi, and D. M. Bouwes, "Light-trapping optimization in wet-etched silicon photonic crystal solar cells," J. Appl. Phys., **118**, 023103 (2015).
5. Y. Fu, Y. Hara, C. W. Miller, and R. Lopez, "Enhancing light absorption within the carrier transport length in quantum junction solar cells," Appl. Opt. **54**, 7933–7939 (2015).
6. W. G. J. H. M. van Sark, K. W. J. Barnham, L. H. Slooff, A. J. Chatten, A. Buchtemann, A. Meyer, S. J. McCormack, R. Koole, D. J. Farrell, R. Bose, E. E. Bende, A. R. Burgers, T. Budel, J. Quilitz, M. Kennedy, T. Meyer, C. D. M. Donega, A. Meijerink, and D. Vanmaekelbergh, "Luminescent solar concentrators—a review of recent results," Opt. Express **16**, 21773–21792 (2008).
7. W. G. J. H. M. van Sark, "Luminescent solar concentrators—a low cost photovoltaics alternative," Renewable Energy **49**, 207–210 (2013).
8. G. Maggioni, A. Campagnaro, S. Carturan, and A. Quaranta, "Dye-doped parylene-based thin film materials: application to luminescent solar concentrators," Solar Energy Mater. Sol. Cells **108**, 27–37 (2013).
9. C.-C. Sun, T.-X. Lee, Y.-C. Lo, C.-C. Chen, and S.-Y. Tsai, "Light extraction enhancement of GaN-based LEDs through passive/active photon recycling," Opt. Commun. **284**, 4862–4868 (2011).
10. S. T. Tan, X. W. Sun, H. V. Demir, and S. P. DenBaars, "Advances in the LED materials and architectures for energy-saving solid-state lighting toward" lighting revolution"," IEEE Photon. J. **4**, 613–619 (2012).
11. M. R. Krames, O. B. Shchekin, R. Mueller-Mach, G. O. Mueller, L. Zhou, G. Harbers, and M. G. Craford, "Status and future of high-power light-emitting diodes for solid-state lighting," J. Disp. Technol. **3**, 160–175 (2007).
12. R. Dylewicz, A. Z. Khokhar, R. Wasielewski, P. Mazur, and F. Rahman, "Nanostructured graded-index antireflection layer formation on GaN for enhancing light extraction from light-emitting diodes," Appl. Phys. B **107**, 393–399 (2012).
13. J. Jewell, D. Simeonov, S.-C. Huang, Y.-L. Hu, S. Nakamura, J. Speck, and C. Weisbuch, "Double embedded photonic crystals for extraction of guided light in light-emitting diodes," Appl. Phys. Lett., **100**, 171105 (2012).
14. X. Sheng, L. Z. Broderick, J. Hu, L. Yang, A. Eshed, E. A. Fitzgerald, J. Michel, and L. C. Kimerling, "Design and fabrication of high-index-contrast self-assembled texture for light extraction enhancement in LEDs," Opt. Express **19**, A701–A709 (2011).
15. O. Heikkila, J. Oksanen, and J. Tulkki, "Light extraction limits in textured GaN-InGaN light-emitting diodes: radiative transfer analysis," Appl. Phys. Lett., **99**, 161110 (2011).
16. P. Zhao and H. Zhao, "Analysis of light extraction efficiency enhancement for thin-film-flip-chip InGaN quantum wells light-emitting diodes with GaN micro-domes," Opt. Express **20**, A765–A776 (2012).

17. M. Moharam and T. Gaylord, "Rigorous coupled-wave analysis of planar-grating diffraction," J. Opt. Soc. Am. **71**, 811–818 (1981).
18. Y. Song, E. Choi, J. Yu, and Y. Lee, "Light-extraction enhancement of red AlGaInP light-emitting diodes with antireflective subwavelength structures," Opt. Express **17**, 20991–20997 (2009).
19. T. X. Lee, C. Y. Lin, S. H. Ma, and C. C. Sun, "Analysis of position-dependent light extraction of GaN-based LEDs," Opt. Express **13**, 4175–4179 (2005).
20. J.-W. Pan and C.-S. Wang, "Light extraction efficiency of GaN-based LED with pyramid texture by using ray path analysis," Opt. Express **20**, A630–A640 (2012).
21. E. K. Kang, E. Kwon, J. W. Min, Y. M. Song, and Y. T. Lee, "Improved light extraction efficiency of GaN-based vertical LEDs using hierarchical micro/subwavelength structures," Jpn. J. Appl. Phys. **54**, 06FH02 (2015).
22. D. Faye, J.-P. Lefevre, J. A. Delaire, and I. Leray, "A selective lead sensor based on a fluorescent molecular probe grafted on a PDMS microfluidic chip," J. Photochem. Photobiol. A **234**, 115–122 (2012).
23. T. Kim, D. Kurunthu, J. J. Burdett, and C. J. Bardeen, "The effects of nanopillar surface texturing on the photoluminescence of polymer films," J. Appl. Phys., **108**, 033114 (2010).
24. B. Ma, S. Wu, and F. Zeng, "Reusable polymer film chemosensor for ratiometric fluorescence sensing in aqueous media," Sens. Actuators B **145**, 451–456 (2010).
25. W. H. Koo, S. M. Jeong, F. Araoka, K. Ishikawa, S. Nishimura, T. Toyooka, and H. Takezoe, "Light extraction from organic light-emitting diodes enhanced by spontaneously formed buckles," Nat. Photonics **4**, 222–226 (2010).
26. L. Xu, J.-W. McGraw, F. Gao, M. Grundy, Z. Ye, Z. Gu, and J. L. Shepherd, "Production of high-concentration graphene dispersions in low-boiling-point organic solvents by liquid-phase noncovalent exfoliation of graphite with a hyperbranched polyethylene and formation of graphene/ethylene copolymer composites," J. Phys. Chem. C **117**, 10730–10742 (2013).
27. T. Q. Nguyen, V. Doan, and B. J. Schwartz, "Conjugated polymer aggregates in solution: control of interchain interactions," J. Chem. Phys. **110**, 4068–4078 (1999).
28. P.-J. Chen, M.-K. Wang, J.-H. Hsu, A. C. M. Yang, and J. D. White, "Observing and modeling light propagation in polymer films," Appl. Phys. Lett., **102**, 143302 (2013).
29. J. A. E. Wasey, A. Safonov, I. D. W. Samuel, and W. L. Barnes, "Effects of dipole orientation and birefringence on the optical emission from thin films," Opt. Commun. **183**, 109–121 (2000).
30. W. Y. Sun, S. C. Yang, J. D. White, J. H. Hsu, K. Y. Peng, S. A. Chen, and W. S. Fann, "Conformation and energy transfer in a single luminescent conjugated polymer," Macromolecules **38**, 2966–2973 (2005).
31. S. J. Lee, "Analysis of light-emitting diodes by Monte Carlo photon simulation," Appl. Opt. **40**, 1427–1437 (2001).
32. P. C. Y. Chang, J. G. Walker, and K. I. Hopcraft, "Ray tracing in absorbing media," J. Quant. Spectrosc. Radiat. Transfer **96**, 327–341 (2005).
33. P. Biagioni, J.-S. Huang, and B. Hecht, "Nanoantennas for visible and infrared radiation," Rep. Prog. Phys., **75**, 024402 (2012).
34. J.-J. Liang, J. D. White, Y. C. Chen, C. F. Wang, J. C. Hsiang, T. S. Lim, W. Y. Sun, J. H. Hsu, C. P. Hsu, M. Hayashi, W. S. Fann, K. Y. Peng, and S. A. Chen, "Heterogeneous energy landscapes of individual luminescent conjugated polymers," Phys. Rev. B, **74**, 085209 (2006).
35. C. C. Sun, C. Y. Lin, T. X. Lee, and T. H. Yang, "Enhancement of light extraction of GaN-based light-emitting diodes with a microstructure array," Opt. Eng. **43**, 1700–1701 (2004).